

Cite this: *J. Mater. Chem. A*, 2026, **14**, 7695

# Thermally-driven chemical heterogeneity produces large thermopower and multiday operability in a thermogalvanic cell

Ehsan Hosseini,<sup>1</sup>  <sup>\*,a</sup> Mohammad Zakertabrizi,<sup>a</sup> Mina Hosseini,<sup>a</sup> Arian Zarriz,<sup>a</sup> Rouzhina Azhdari<sup>a</sup> and Matthew. J. Powell-Palm<sup>\*,abc</sup>

Thermogalvanic cells, which convert low-grade heat into electricity, usually employ chemically-homogeneous electrolytes that limit the Seebeck response to redox entropy alone. Here, we introduce a redox-split thermogalvanic cell in which a temperature gradient drives localized oxidation of a nickel-bipyridine complex at the hot electrode only, creating chemical heterogeneity that augments thermopower *via* additional concentration gradient effects. We add weakly coordinating anions to stabilize the oxidized species, increase redox entropy change, and balance electrical and thermal transport, and the optimized cell delivers a Seebeck coefficient of 6.44 mV K<sup>-1</sup>; a maximum power density  $\sim 8$  W m<sup>-2</sup>; and  $\sim 0.5$  V (open circuit) at a 75 K gradient. It furthermore supplies power for >8 days under load with  $\sim 8\%$  relative Carnot efficiency and a figure of merit  $ZT \sim 0.8$ , offering a durable, efficient route towards waste heat recovery.

Received 13th November 2025  
Accepted 15th January 2026

DOI: 10.1039/d5ta09239f

rsc.li/materials-a

## Introduction

Thermogalvanic cells (TGCs) are electrochemical systems capable of converting thermal energy from temperature gradients directly into electrical power, through the interplay of one or more redox couples.<sup>1</sup> When a temperature gradient is applied across two electrodes in contact with a redox-active electrolyte, the resulting imbalance in electrochemical potentials gives rise to a thermally-induced voltage, the magnitude of which is typically quantified by the Seebeck coefficient ( $S_e$ ).<sup>2-5</sup>

Based on the Nernst equation, the Seebeck coefficient ( $S_e$ ) in TGCs arises from two principal thermodynamic contributions (see Supplementary Note 1 for theoretical treatment). One is the solvation-structural entropy difference ( $\Delta S$ ) between the oxidized and reduced states of the redox couple, governed by factors such as charge density, molecular geometry, and flexibility, which are reflected in the solvation shell surrounding the species. Subtle rearrangements of hydrogen-bonding networks or solvation shells can strongly influence the entropy of each redox species (and the entropic difference between them), thereby amplifying the thermoelectric response.<sup>6-9</sup>

The second contribution comes from the difference in reductant-to-oxidant concentration ratio within the electrolyte at the cold electrode *vs.* the hot ( $\Delta C_r$ ). While non-zero  $\Delta C_r$  values

represent chemical heterogeneity and typically decay spontaneously *via* diffusive mixing, leading to  $\Delta C_r \approx 0$  at steady state, recent studies demonstrate that concentration differences can be engineered into thermogalvanic cells through various means, thereby producing  $S_e$  values that surpass conventional limits by leveraging the additive contributions of chemical heterogeneity and reductant-oxidant entropy difference.<sup>10-14</sup>

Despite these advances, most conventional TGCs fail to utilize chemical heterogeneity to their advantage, instead accepting spatially homogeneous distributions of redox species that limit accessible entropy change and accordingly restrict the Seebeck response. Cells incorporating tough gel matrices or segregated crystalline phases present a notable exception to this trend, either slowing the equilibration of concentration gradients<sup>15,16</sup> or sustaining them permanently by physical means.<sup>12,17-19</sup> However, while these systems underscore the potential of exploiting  $\Delta C_r$  to exceed the intrinsic  $\Delta S$  contribution of conventional redox pairs,<sup>12</sup> production of stable chemical heterogeneity in fully-liquid thermogalvanic cells, which present the broadest canvas for molecular design of the many other properties affecting thermogalvanic performance (*e.g.* thermal operating window,<sup>20-22</sup> thermal conductivity, electrical conductivity), has not yet been reported.<sup>11</sup>

Here, we utilize the nickel-bipyridine complex  $[\text{Ni}(\text{bpy})_3]^{2+}/[\text{Ni}(\text{bpy})_3]^{13+}$  in a non-aqueous electrolyte to introduce a unique mode of stable thermal-to-electrical energy conversion based on temperature-dependent liquid-phase chemical heterogeneity, which we realize in a cell design we dub a Redox-Split Thermogalvanic Cell (RS-TGC). In our optimized RS-TGC, the reductant  $[\text{Ni}(\text{bpy})_3]^{2+}$  is the dominant species in the nonaqueous electrolyte and the only redox species present under isothermal conditions, while application of a thermal

<sup>a</sup>J. Mike Walker '66 Dept. of Mechanical Engineering, Texas A&M University, College Station, TX 77803, USA. E-mail: ehsan.hosseini@tamu.edu; powellpalm@tamu.edu

<sup>b</sup>Dept. of Materials Science and Engineering, Texas A&M University, College Station, TX 77803, USA

<sup>c</sup>Dept. of Biomedical Engineering, Texas A&M University, College Station, TX 77803, USA



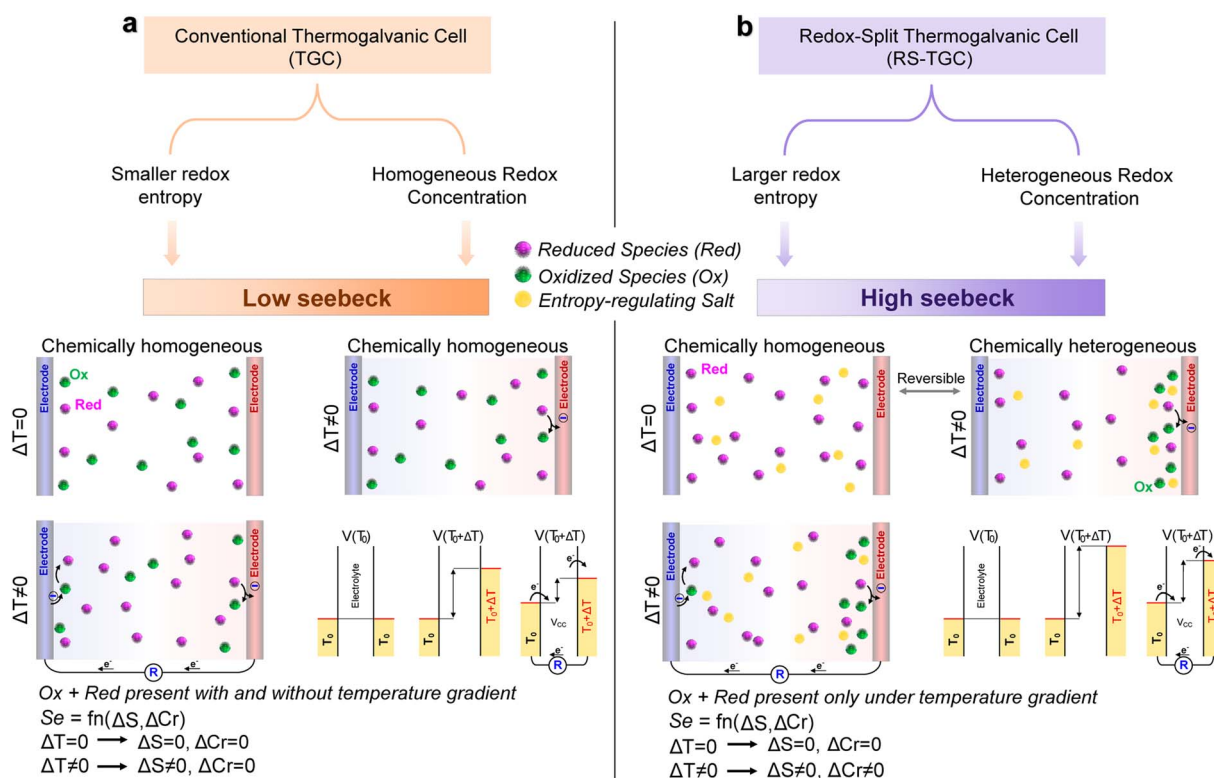
gradient drives localized formation of the oxidant  $[\text{Ni}(\text{bpy})_3]^{3+}$  only at the hot (negative) electrode. This thermally-induced redox partitioning defies the homogeneous character of conventional thermogalvanic systems, and generates a Seebeck-enhancing chemically heterogeneous state that appears only under a temperature gradient. We then couple this heterogeneity with entropy-regulating salts that both selectively affect and stabilize  $[\text{Ni}(\text{bpy})_3]^{3+}$  (increasing both the redox entropy difference and the thermo-chemical heterogeneity) and enhance electrical conductivity, in a non-aqueous electrolyte chosen both for its solvation behaviors with  $[\text{Ni}(\text{bpy})_3]^{2+}/[\text{Ni}(\text{bpy})_3]^{3+}$  and for its low thermal conductivity. This combination of stable electrode-to-electrode concentration gradients, selectively enhanced redox entropy differences, and favorable electronic and thermal transport properties yields a liquid-phase thermogalvanic cell with both remarkable efficiency and as-yet unreported longevity (able to operate under load for >1 week without change), establishing RS-TGCs as a promising platform for low-grade heat harvesting.

## Results

In Fig. 1, we compare essential conceptual characteristics of conventional and redox-split thermogalvanic cells. As shown in Fig. 1a, given the comparable stability of the reductants and

oxidants used in conventional TGCs, these cells maintain approximately homogeneous redox distributions under both isothermal conditions and thermal gradients, which limit contributions to the Seebeck coefficient to those that stem from redox entropy differences. By contrast, Fig. 1b illustrates that RS-TGCs undergo thermally-induced partitioning: while  $[\text{Ni}(\text{bpy})_3]^{2+}$  is the only species stable under isothermal conditions,<sup>23–25</sup>  $[\text{Ni}(\text{bpy})_3]^{3+}$  is selectively stabilized at the hot (negative) electrode under a temperature gradient, creating chemical heterogeneity that increases the entropy difference between electrodes and enhances thermopower. This effect originates from the distinct temperature-dependent solvation dynamics of  $[\text{Ni}(\text{bpy})_3]^{2+}$  and  $[\text{Ni}(\text{bpy})_3]^{3+}$ , and may be further enhanced by entropy-regulating anions such as  $\text{PF}_6^-$  and  $\text{TFSI}^-$  (as we will demonstrate below), which provide a weakly coordinating, charge-diffuse environment that preferentially stabilizes  $[\text{Ni}(\text{bpy})_3]^{3+}$ , amplifying both the solvation-entropy difference ( $\Delta S$ ) between redox species and the concentration ratio difference ( $\Delta C_r$ ) between electrodes.

In Fig. 2a, we provide a more detailed operational illustration of our RS-TGC cell, absent additives beyond a non-aqueous electrolyte and the redox pair. We employ tris(2,2'-bipyridine) nickel(II) bromide as the precursor of  $[\text{Ni}(\text{bpy})_3]^{2+}$  in a non-aqueous solvents, where  $[\text{Ni}(\text{bpy})_3]^{2+}$  persists as the predominant species in the absence of a temperature gradient.<sup>23,25,26</sup>



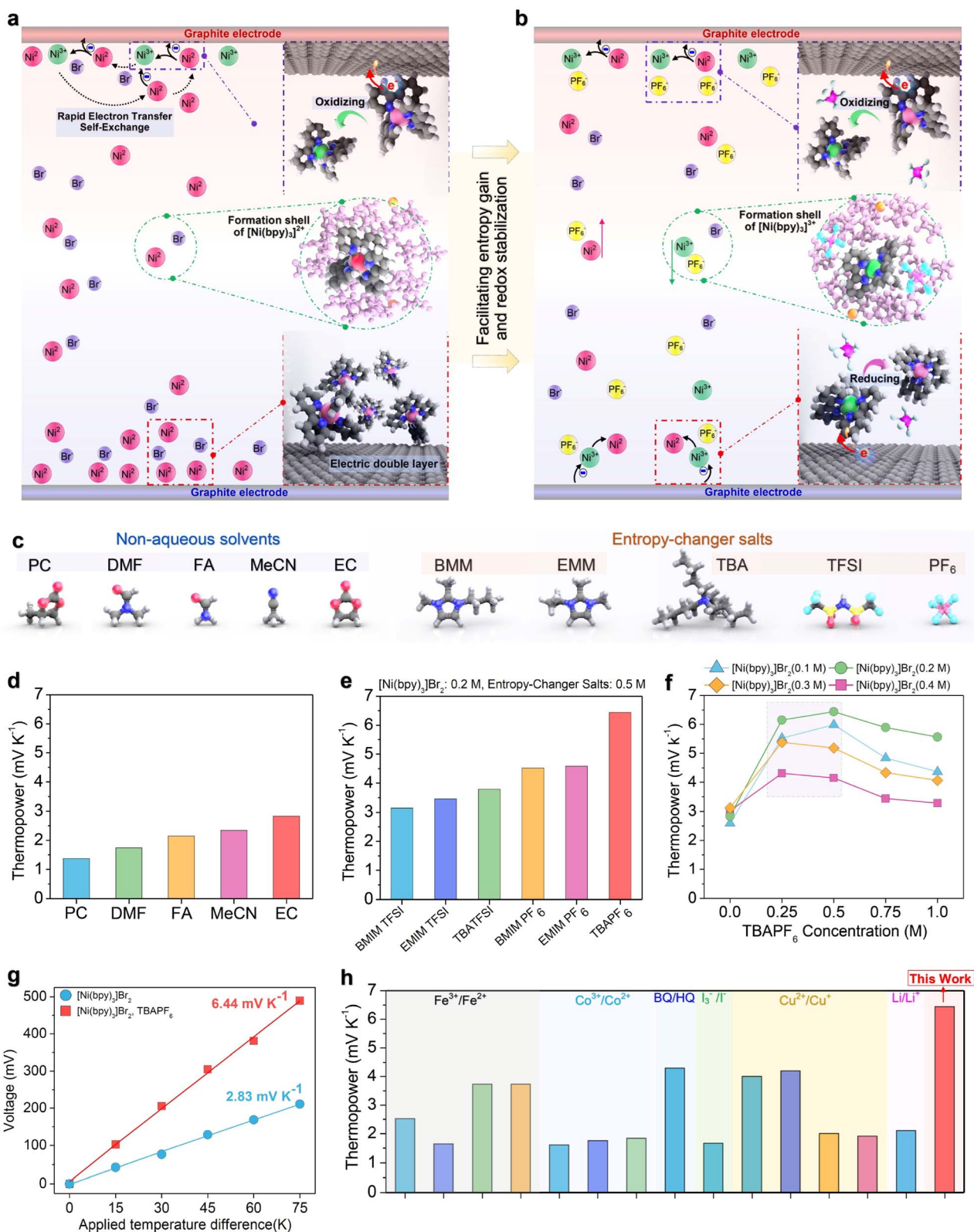


Fig. 2 Characteristics of a redox-split thermogalvanic cell based on  $[\text{Ni}(\text{bpy})_3]^{2+}/^{3+}$  in non-aqueous media. (a) Illustration of  $[\text{Ni}(\text{bpy})_3]^{2+}$  oxidation at the hot electrode without salt, where  $\text{Ni}(\text{III})$  remains unstable. (b) Illustration with  $[\text{TBA}][\text{PF}_6]$ , where ligand substitution is suppressed and  $\text{Ni}(\text{III})$  is stabilized. (c) Molecular structures of the investigated non-aqueous solvents (PC, DMF, FA, MeCN, EC) and salts ( $[\text{BMM}][\text{TFSI}]$ ,  $[\text{EMM}][\text{TFSI}]$ ,  $[\text{TBA}][\text{TFSI}]$ ,  $[\text{BMM}][\text{PF}_6]$ ,  $[\text{EMM}][\text{PF}_6]$ ,  $[\text{TBA}][\text{PF}_6]$ ). (d) Seebeck coefficients of  $[\text{Ni}(\text{bpy})_3]^{2+}/^{3+}$  measured in different solvents. (e) Effect of salt additives in EC, comparing  $\text{PF}_6^-$  and  $\text{TFSI}^-$  based salts. (f) Dependence of the Seebeck coefficient on  $[\text{TBA}][\text{PF}_6]$  concentration for different concentrations of  $[\text{Ni}(\text{bpy})_3]^{2+}/^{3+}$ . (g) Voltage as a function of temperature gradient between cold and hot electrodes for the redox-split thermogalvanic cell, measured with and without  $[\text{TBA}][\text{PF}_6]$ . (h) Comparison of Seebeck coefficients of  $[\text{Ni}(\text{bpy})_3]^{2+}/^{3+}$  with other redox couples under similar measurement conditions.



When a gradient is applied, oxidation occurs preferentially at the hot (negative) graphite or platinum electrode to generate  $[\text{Ni}(\text{bpy})_3]^{3+}$ . In coordinating media with anions such as  $\text{Br}^-$ , the  $\text{Ni}(\text{III})$  state is unstable and rapidly relaxes back to  $[\text{Ni}(\text{bpy})_3]^{2+}$  (see cyclic voltammetry in Fig. S1a; blue curve), restricting oxidation to the hot (negative) electrode interface. This transient and localized redox splitting generates both a  $\Delta S$  and a  $\Delta C\Box$  between electrodes, producing a Seebeck effect greater than that of conventional thermogalvanic cells.

As illustrated in Fig. 2b, this effect may be enhanced further if the otherwise-ephemeral  $\text{Ni}(\text{III})$  state may be additionally stabilized (facilitating both electrode-to-electrode redox exchange and increased  $\Delta C\Box$ ), and if the characteristic entropy difference between this state and  $[\text{Ni}(\text{bpy})_3]^{2+}$  may be further increased. To this end, we next investigated the addition of a variety of entropy regulating salts and the use of an array of non-aqueous solvents, the molecular structures of which are shown in Fig. 2c. Solvents investigated include propylene carbonate (PC), *N,N*-dimethylformamide (DMF), formamide (FA), acetonitrile (MeCN), and ethylene carbonate (EC), and salts include  $[\text{BMIM}][\text{TFSI}]$ ,  $[\text{EMIM}][\text{TFSI}]$ ,  $[\text{TBA}][\text{TFSI}]$ ,  $[\text{BMIM}][\text{PF}_6]$ ,  $[\text{EMIM}][\text{PF}_6]$ , and  $[\text{TBA}][\text{PF}_6]$ .

In Fig. 2d, we show the Seebeck coefficients of  $[\text{Ni}(\text{bpy})_3]\text{Br}_2$  at its optimal concentrations (established in preliminary work and reported in the Methods section) in different non-aqueous solvents, which range from  $1.37 \text{ mV K}^{-1}$  at 0.05 M in PC to  $2.83 \text{ mV K}^{-1}$  at 0.2 M in EC (see Fig. S2 for additional  $[\text{Ni}(\text{bpy})_3]\text{Br}_2$  concentrations in EC). Consistent with previous observations in non-aqueous electrolytes,<sup>27–31</sup> the general trends observed may be explained qualitatively by two dominant factors: (i) the strength of the solvation shell around  $[\text{Ni}(\text{bpy})_3]^{2+}$  and  $[\text{Ni}(\text{bpy})_3]^{3+}$  and (ii) the dielectric screening of charge. PC and DMF form weak solvation shells for both redox species, so entropy change upon redox is minimal. FA, despite being highly polar, stabilizes both redox states strongly, preventing desolvation and similarly suppressing the redox entropy change ( $\Delta S$ ). Furthermore, its high dielectric constant likely screens electrostatic interactions, reducing the potential for concentration imbalance ( $\Delta C\Box$ ). MeCN and EC provide the most suitable environments, structurally stabilizing one redox species ( $\text{Ni}(\text{II})$ ) while still allowing partial desolvation of the other ( $\text{Ni}(\text{III})$ ), thereby providing maximal entropy change upon redox.

Identifying EC as the most optimal non-aqueous electrolyte, in Fig. 2e, we demonstrate the role of entropy-regulating salts in this solvent, with 0.2 M  $[\text{Ni}(\text{bpy})_3]\text{Br}_2$  and 0.5 M salt shown for each solution. While every salt tested enhanced the Seebeck coefficient relative to baseline (0.2 M  $[\text{Ni}(\text{bpy})_3]\text{Br}_2$  in EC),  $[\text{TBA}][\text{PF}_6]$  provided exceptional enhancement, more than doubling  $S_e$  to  $6.44 \text{ mV K}^{-1}$ . Voltage vs. applied temperature differences curves are shown for all solvents and salts in SI Fig. S3 and S4.

Anions such as  $\text{PF}_6^-$  and  $\text{TFSI}^-$  are large, weakly coordinating species in the formation shell, which can suppress ligand substitution and decomposition.<sup>32,33</sup> The pairing of such ions reduces the number of strongly bound solvent molecules around redox molecules, leading to partial desolvation that may disrupt the ordered solvent structure and produce a positive

entropy contribution. These effects are consistent with prior studies on transition-metal bipyridine complexes in ionic liquids, which reported sluggish yet stable Ni-based redox kinetics in electrochemical tests, attributed to large inner-sphere reorganization energies.<sup>34,35</sup>

We hypothesize in particular that  $\text{PF}_6^-$  exhibits superior performance by stabilizing  $[\text{Ni}(\text{bpy})_3]^{3+}$  and enhancing entropy change through partial desolvation of the trication ( $\text{Ni}^{3+}$ ), while suppressing ligand substitution. We interrogate these effects in greater detail with the aid of molecular simulations in Fig. 3. In Fig. S5, we give UV-Vis spectra of  $[\text{Ni}(\text{bpy})_3]^{2+}$  with  $\text{PF}_6^-$  in one nonaqueous electrolyte (ethylene carbonate), showing decreased absorbance intensity and slight broadening of the  $\sim 300 \text{ nm}$  band, and indicating that  $\text{PF}_6^-$  perturbs the solvation environment and modifies the coordination shell. Cyclic voltammetry and UV-Vis spectra (Fig. S1–S7) provides additional direct evidence for the role of  $\text{PF}_6^-$  in facilitating the  $[\text{Ni}(\text{bpy})_3]^{2+}/^{3+}$  redox process and stabilizing  $[\text{Ni}(\text{bpy})_3]^{3+}$  in nonaqueous electrolytes, consistent with previous studies that have shown that the presence of fluorinated anions creates coordination environments favorable for stabilizing this complex cation.<sup>27,29–31,34,36</sup> We note that Fig. S1a also indicates that in the presence of this anion, while ( $\text{Ni}^{3+}$ ) is stabilized relative to its unstable baseline form, the oxidation reaction is still heavily favored over the reduction reaction, and thus will not disrupt (and may plausibly enhance) the chemical heterogeneity between electrodes.

Fig. 2f shows the dependence of the Seebeck coefficient on  $[\text{TBA}][\text{PF}_6]$  concentration for varying concentrations of  $[\text{Ni}(\text{bpy})_3]\text{Br}_2$ . The optimum range is between 0.25 and 0.5 M, where incorporation of  $\text{PF}_6^-$  into the coordination/formation shell of  $[\text{Ni}(\text{bpy})_3]^{2+}/^{3+}$  effectively disrupts the shell structure and enhances ion mobility. At higher  $[\text{TBA}][\text{PF}_6]$  concentrations, however, excess  $\text{PF}_6^-$  anions accumulate in the solvation shell, reducing the  $\Delta S$  and thereby lowering the Seebeck coefficient (Fig. S8). In Fig. 2g, we compare the open-circuit thermopower in our optimal RS-TGC (0.2 M  $[\text{Ni}(\text{bpy})_3]\text{Br}_2$  in EC) with and without  $[\text{TBA}][\text{PF}_6]$ , with the cold side fixed at  $313.15 \text{ K}$  to maintain the cell in its liquid phase at all times. The slopes of these curves correspond to the Seebeck coefficient, and both the pristine and salt-enhanced RS-TGCs maintain linearity of voltage over a wide range of temperature deltas (up to  $dT = 75^\circ \text{ C}$ ). This range exceeds that available to most conventional thermogalvanic cells, and further demonstrates the stability of the RS-TGC mechanism.

In order to contextualize the remarkable the thermopower of the optimized RS-TGC, we benchmarked its measured Seebeck coefficient against several conventional thermogalvanic cells (TGCs) in Fig. 2f, including cells based on  $\text{Fe}^{3+}/\text{Fe}^{2+}$ ,  $\text{Co}^{3+}/\text{Co}^{2+}$ , benzoquinone/hydroquinone,  $\text{I}^-/\text{I}_3^-$ ,  $\text{Cu}^{2+}/\text{Cu}^+$ , and  $\text{Li}^+/\text{Li}$ . Most established systems exhibit Seebeck coefficients below  $3 \text{ mV K}^{-1}$ , and even entropy-enriched couples such as BQ/HQ or  $\text{I}^-/\text{I}_3^-$  generally remain in the range of  $4\text{--}5 \text{ mV K}^{-1}$ . By contrast, the  $[\text{Ni}(\text{bpy})_3]^{2+}/^{3+}$  system in EC with  $[\text{TBA}][\text{PF}_6]$  achieves  $6.44 \text{ mV K}^{-1}$ , representing one of the highest redox thermopower values reported for thermogalvanic systems.



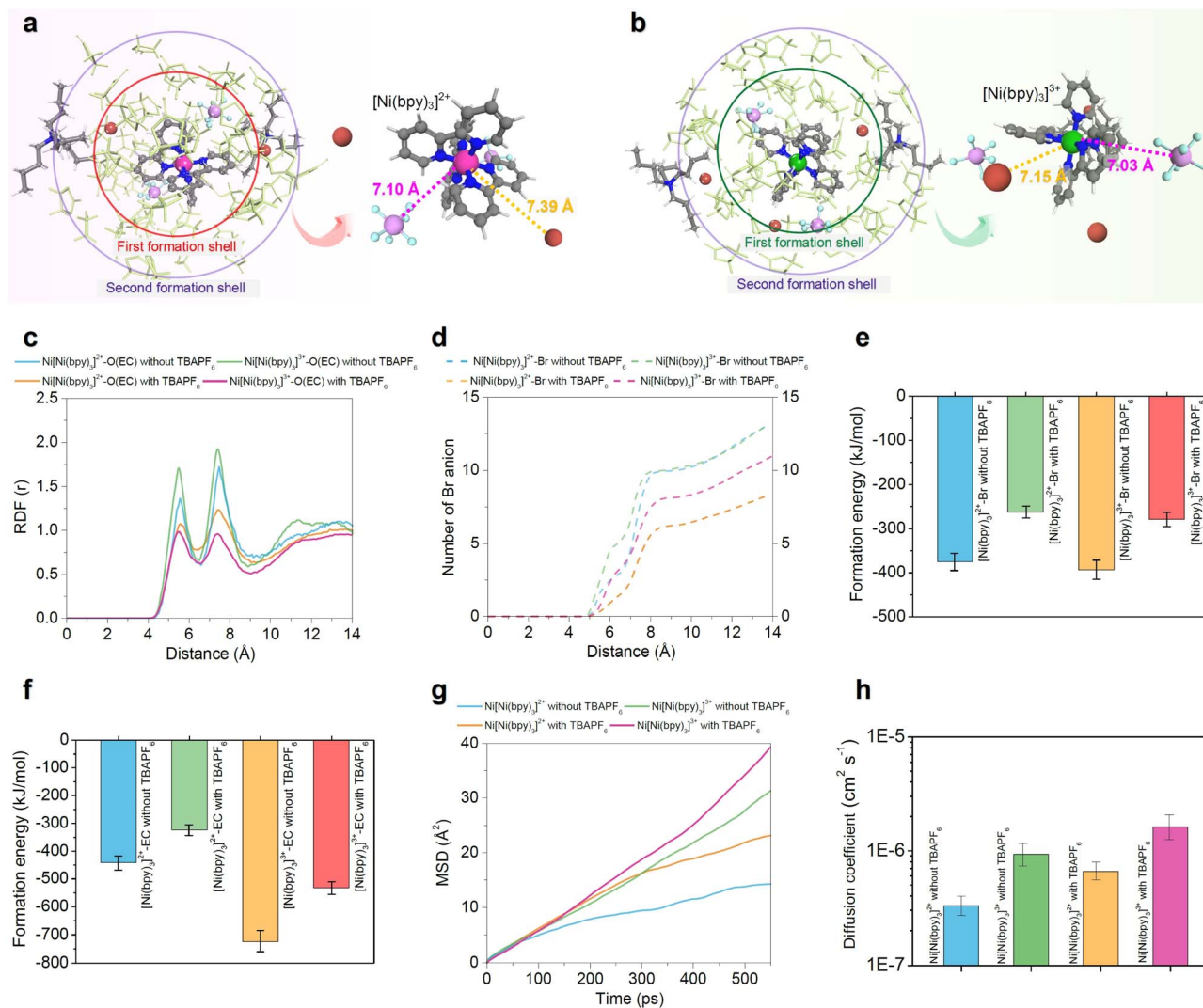


Fig. 3 Molecular dynamics simulations and thermodynamic analysis of [Ni(bpy)<sub>3</sub>]<sup>2+</sup>/<sup>3+</sup> in ethylene carbonate with and without PF<sub>6</sub><sup>-</sup>. Snapshots of [Ni(bpy)<sub>3</sub>]<sup>2+</sup> and [Ni(bpy)<sub>3</sub>]<sup>3+</sup> (a and b) illustrate the first and second formation shells, showing that PF<sub>6</sub><sup>-</sup> ions displace Br<sup>-</sup> and disturb the ordering of nearby solvent molecules. Radial distribution functions of Ni–O(EC) distances. (c) Reveal weaker and less localized coordination in the presence of PF<sub>6</sub><sup>-</sup>, while coordination number analysis (d) confirms a reduction in Br<sup>-</sup> occupancy near the complexes. Formation energy calculations for Ni–Br (e) and Ni–EC interactions (f) show a consistent reduction in binding strength under PF<sub>6</sub><sup>-</sup> regulation, supporting disruption of rigid ion–solvent cages. Mean square displacement traces (g) and diffusion coefficients (h) demonstrate that PF<sub>6</sub><sup>-</sup> loosens the solvation cages and enhances translational motion of the complexes in the bulk electrolyte. Together, these structural, dynamic, and energetic results establish that PF<sub>6</sub><sup>-</sup> acts as an entropy-regulating anion, destabilizing compact solvation shells, promoting partial desolvation, and increasing molecular freedom, thereby amplifying the entropy difference between [Ni(bpy)<sub>3</sub>]<sup>2+</sup> and [Ni(bpy)<sub>3</sub>]<sup>3+</sup>.

Furthermore, as detailed in the following sections, this system not only establishes a record Seebeck coefficient but also demonstrates operational stability (open circuit and under load) for periods ~100× times longer than most conventional TGCs. In Fig. S9, we also demonstrate the performance of the cell across different electrode materials (graphite sheet, graphite felt, carbon cloth, and platinum) at maximum  $\Delta T$  (75 K), all of which show similarly high Seebeck values (~6–6.44 mV K<sup>-1</sup>, with graphite sheet electrodes performing best).

To investigate the molecular origin of the significant entropy change of the [Ni(bpy)<sub>3</sub>]<sup>2+</sup>/<sup>3+</sup> couple in our RS-TGC, we performed molecular dynamics (MD) and density functional theory (DFT) simulations in an ethylene carbonate medium containing

[TBA][PF<sub>6</sub>]. Snapshots in Fig. 3a and b illustrate the first and second solvation shells surrounding [Ni(bpy)<sub>3</sub>]<sup>2+</sup> and [Ni(bpy)<sub>3</sub>]<sup>3+</sup>. The PF<sub>6</sub><sup>-</sup> ions approach the metal center, frequently displacing Br<sup>-</sup> and disrupting the ordered network of EC molecules. At a trend level, this exchange weakens the structured solvation shells around both Ni(II) and Ni(III), with a particularly strong effect for the trivalent complex. As a result, specific Ni–Br interactions are diminished and solvent molecules that were previously constrained in the coordination shell are released back into the bulk, producing greater shell disorder and amplifying the configurational entropy difference between the two redox states. These trends are quantified in Fig. 3c–h. In Fig. 3c, we show radial distribution functions (RDF) between Ni



and O(EC) with and without  $\text{PF}_6^-$ . The addition of  $\text{PF}_6^-$  produces a substantial decrease in peak intensity, indicating reduction of strongly bound EC molecules and disordering of the solvation shell. Critically, this decrease is markedly more pronounced for  $\text{Ni(III)}$  (where  $\text{PF}_6^-$  pairing is strongest) as compared to  $\text{Ni(II)}$ , suggesting differential solvation effects between oxidant and reductant that necessarily increase the redox entropy change. Fig. 3d shows the coordination number of  $\text{Br}^-$  ions located within the formation shells of  $[\text{Ni}(\text{bpy})_3]^{2+}$  and  $[\text{Ni}(\text{bpy})_3]^{3+}$  (Fig. S10). In the electrolyte without  $\text{PF}_6^-$ , the average numbers of  $\text{Br}^-$  near the complexes are about five for  $[\text{Ni}(\text{bpy})_3]^{2+}$  and about seven for  $[\text{Ni}(\text{bpy})_3]^{3+}$  (within a radius of  $\sim 7 \text{ \AA}$ ). When  $\text{PF}_6^-$  is introduced, these values decrease by nearly half, indicating that  $\text{PF}_6^-$  replaces  $\text{Br}^-$  in the near-metal region and leads to a more complete separation of the redox pair at the atomic scale.

The disruptive effects of  $\text{PF}_6^-$  on the solvation shells  $[\text{Ni}(\text{bpy})_3]^{2+}$  and  $[\text{Ni}(\text{bpy})_3]^{3+}$  are furthermore evident in the

formation energies of each species with  $\text{Br}^-$  ions and EC molecules (Fig. 3e and f), all of which are reduced significantly in magnitude upon introduction of the salt. By weakening strong Ni–Br and Ni–O(EC) interactions,  $\text{PF}_6^-$  increases the configurational degrees of freedom of the system, and thereby the configurational entropy change possible upon redox. The characteristic signature of this enhanced configurational freedom may also be seen in the mean square displacement (MSD) of the redox species, from which diffusion coefficients may be extracted (Fig. 3g and h). Diffusion coefficients of both  $[\text{Ni}(\text{bpy})_3]^{2+}$  and  $[\text{Ni}(\text{bpy})_3]^{3+}$  nearly double in the presence of  $\text{PF}_6^-$ , implying not only that it disrupts the  $[\text{Ni}(\text{bpy})_3]^{2+/3+}$  solvation shells and increases the redox entropy difference, as supported by Fig. 3g and h, but also yields broadly faster transport kinetics for the redox pair, which may further benefit thermogalvanic performance.

We also note that  $[\text{Ni}(\text{bpy})_3]$  complexes themselves, absent any additives, experience intrinsically large entropy changes

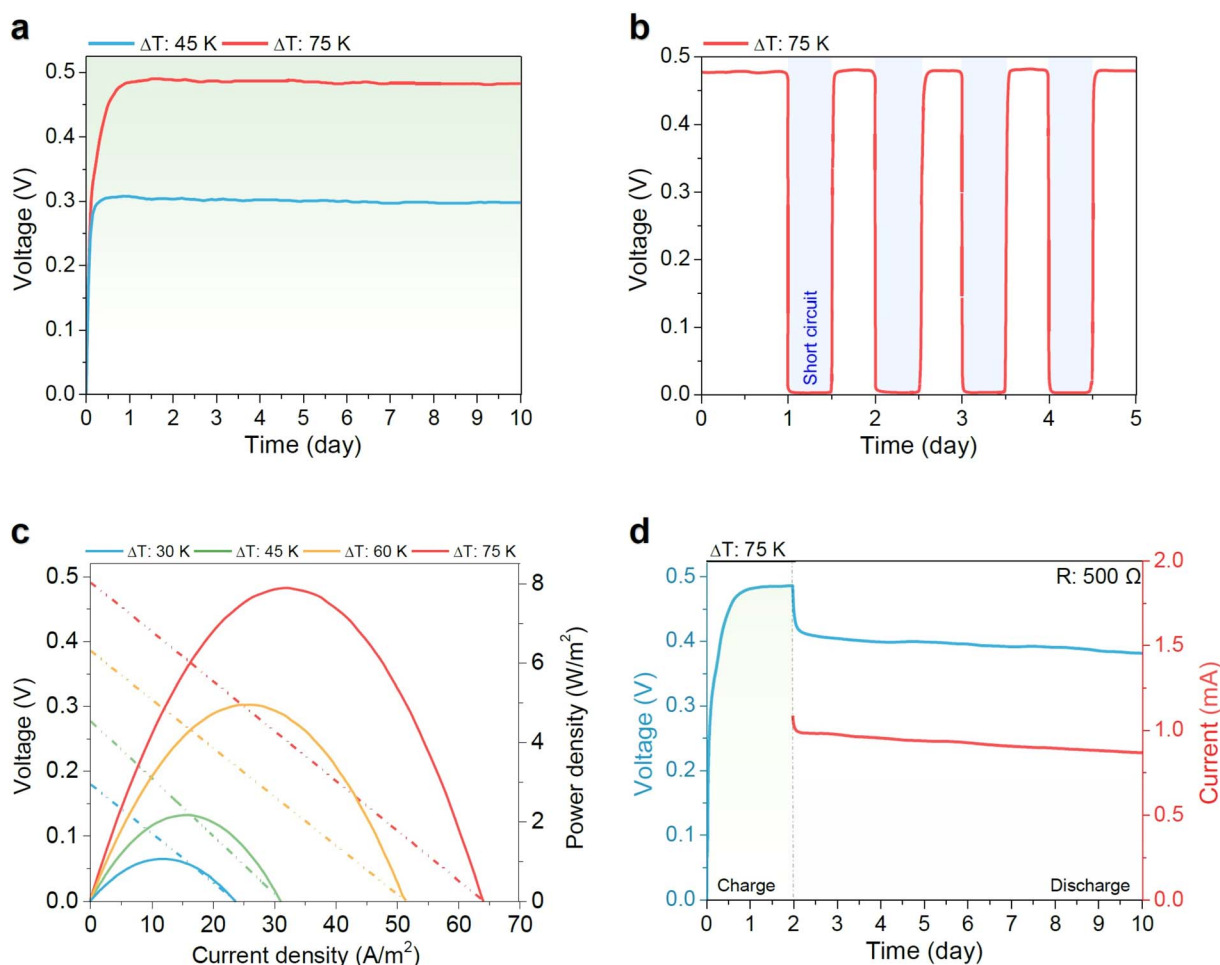


Fig. 4 Multiday Operability and performance optimization of  $[\text{Ni}(\text{bpy})_3]^{2+/3+}$  thermogalvanic cells. Thermogalvanic cells were prepared with 0.2 M tris(2,2'-bipyridine)nickel bromide and 0.5 M [TBA][ $\text{PF}_6$ ] in ethylene carbonate and tested for long-term stability and practical performance. (a) Long-term voltage stability at  $\Delta T = 45 \text{ K}$  and  $75 \text{ K}$ , showing continuous operation for more than ten days. (b) Cycling stability under repeated short-circuit and recovery at  $\Delta T = 75 \text{ K}$ , demonstrating reproducible voltage response during repeated perturbations. (c) Current–voltage and power–density characteristics recorded at increasing temperature gradients, illustrating systematic enhancement of thermoelectric output as  $\Delta T$  increases. (d) Charge–discharge performance under a  $500 \Omega$  load at  $\Delta T = 75 \text{ K}$ , highlighting continuous and stable power delivery maintained over extended operation.



upon redox, based on vibrational differences between reductant and oxidant. Our DFT calculations (Fig. S11) show that the transition from  $[\text{Ni}(\text{bpy})_3]^{2+}$  to  $[\text{Ni}(\text{bpy})_3]^{3+}$  corresponds to an electronic reorganization from  $(\text{nd})^6(\text{ad})^2(\text{d}^8)$  to  $(\text{nd})^6(\text{ad})^1(\text{d}^7)$ , *i.e.*, the removal of an antibonding electron. This orbital change produces a significant structural contraction of the coordination environment, with average Ni–N bond lengths decreasing from  $\sim 2.091$  Å in  $[\text{Ni}(\text{bpy})_3]^{2+}$  to  $\sim 1.985$  Å in  $[\text{Ni}(\text{bpy})_3]^{3+}$  (Ni–N bonds contract strongly  $\approx 0.11$  Å, or a  $\sim 5\%$  decrease).<sup>47</sup> For comparison, for  $(\text{Fe}(\text{CN})_6)^{3-}$ , the Fe–C bond length is  $\sim 1.96$  Å, whereas in  $(\text{Fe}(\text{CN})_6)^{4-}$  it is  $\sim 1.94$  Å, giving a much smaller contraction of  $\approx 0.02$  Å (a  $\sim 1\%$  decrease) (Fig. S11). This bond shortening in the oxidation state intensifies vibrational contributions to the entropy, generating additional entropy change during the redox process. As such, we hypothesize that this synergy between solvation-shell disorder, driven by  $\text{PF}_6^-$  substitution, and vibrational reorganization of the Ni–N coordination bonds accounts for the unusually large entropy change (and accordingly Seebeck coefficient) observed in the system.

This mechanistic molecular picture developed in Fig. 2 and 3 is directly reflected in device-level performance, which we evaluated *via* many-days-long testing of the optimized RS-TGC (containing 0.2 M tris(2,2'-bipyridine)nickel bromide and 0.5 M [TBA][PF<sub>6</sub>] in EC). First, in Fig. 4a we demonstrate long-term open-circuit stability for more than 9 days, maintaining  $\sim 0.32$  V at  $\Delta T = 45$  K and  $\sim 0.50$  V at  $\Delta T = 75$  K in a single cell without perceptible degradation. The observed  $\sim 0.50$  V

surpasses conventional TGCs such as  $\text{Fe}^{3+}/\text{Fe}^{2+}$ ,  $\text{Co}^{3+}/\text{Co}^{2+}$ , and  $\text{I}^-/\text{I}_3^-$ , which generally achieve  $\leq 0.2$  V, and exhibits remarkable durability with time.<sup>20,25,48–50</sup> Under repeated short-circuit cycling (Fig. 4b), this voltage consistently recovers to its steady-state value, further confirming that the voltage is driven by stable redox, as opposed to ephemeral thermodiffusion processes. Fig. S12 shows that under  $\Delta T = 75$  K (open circuit), the cell exhibits a slow voltage build-up, requiring  $\sim 0.5$ –1 day to reach a plateau, and that when  $\Delta T$  is removed, the voltage relaxes back to zero over  $\sim 2$  days, consistent with the back-conversion of  $[\text{Ni}(\text{bpy})_3]^{3+}$  to  $[\text{Ni}(\text{bpy})_3]^{2+}$  and the dissipation of both concentration and entropy gradients. Performance characterization with increasing temperature gradient (Fig. 4c) demonstrates smooth scaling of current–voltage and power density characteristics, with the system reaching  $\sim 500$  mV open-circuit potential,  $\sim 8$  W m<sup>-2</sup> maximum power density, and  $\sim 65$  A m<sup>-2</sup> peak current density at  $\Delta T = 75$  K. Electrode comparison further shows that graphite felt delivers the highest output ( $\sim 8$  W m<sup>-2</sup>), carbon cloth follows closely ( $\sim 7.5$  W m<sup>-2</sup>), while graphite plate and platinum electrodes achieve only  $\sim 3.5$  W m<sup>-2</sup> due to their lower surface areas (Fig. S13).

In order to demonstrate both the potential practical utility of the optimized cell and its continuous redox nature, we proceeded to conduct multi-day thermal-electric energy conversion under a 500 Ω load. Fig. 4d shows continuous delivery of  $\sim 0.45$  V and  $\sim 0.9$  mA for more than 8 days uninterrupted, far exceeding conventional thermogalvanic systems, where output

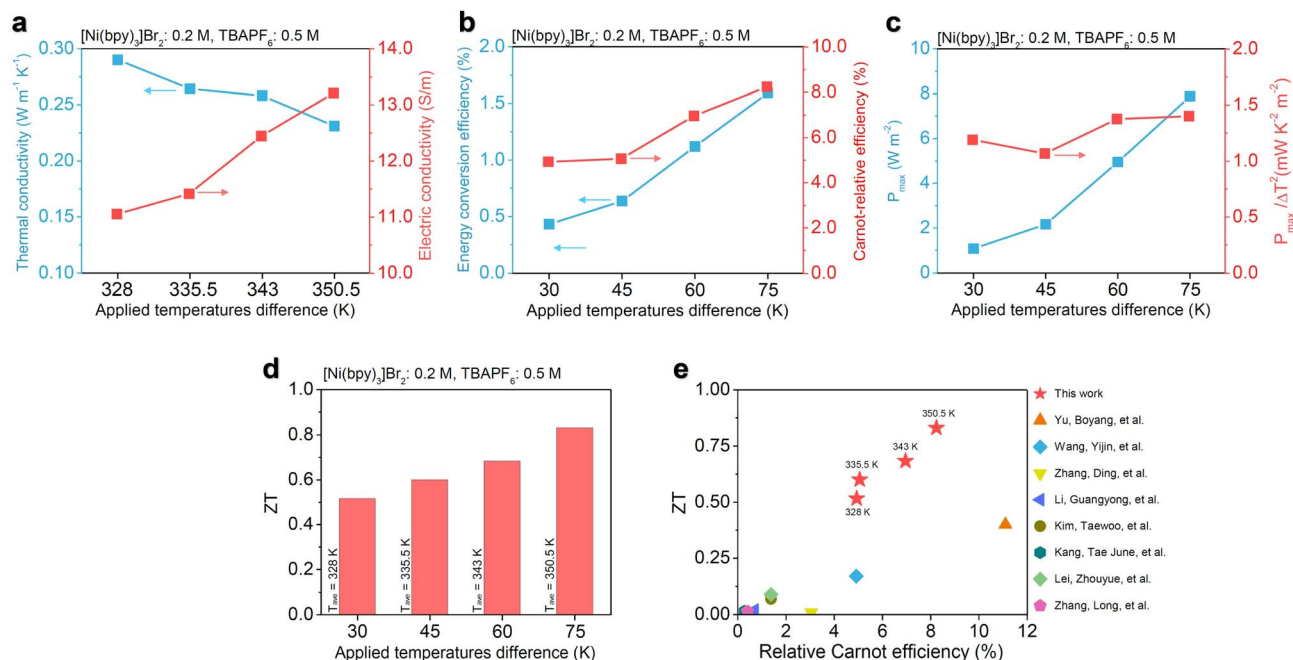


Fig. 5 Transport properties, efficiency, and figure of merit of redox-split  $[\text{Ni}(\text{bpy})_3]^{2+/3+}$  thermogalvanic cells. Thermogalvanic cells were prepared with 0.2 M  $[\text{Ni}(\text{bpy})_3]\text{Br}_2$  and 0.5 M [TBA][PF<sub>6</sub>] in ethylene carbonate to evaluate transport balance, efficiency, and performance metrics. (a) Thermal conductivity and electrical conductivity as a function of applied temperature difference, showing decreasing thermal conductivity and increasing electrical conductivity between  $\Delta T = 30$ –75 K. (b) Energy conversion efficiency and Carnot-relative efficiency as  $\Delta T$  increases, showing systematic improvement with higher temperature gradients. (c) Maximum power density and normalized  $P_{\text{max}}/\Delta T^2$ , demonstrating intrinsic performance enhancement with increasing  $\Delta T$ . (d) Thermoelectric figure of merit (ZT) as a function of  $\Delta T$ , showing steady improvement across the applied temperature range. (e) Comparison of ZT and relative Carnot efficiency across different thermogalvanic systems, where the  $[\text{Ni}(\text{bpy})_3]^{2+/3+}$  couple lies in the high-ZT, high-efficiency regime relative to conventional aqueous redox couples.<sup>4,12,54–59</sup>



typically decays within minutes (Table. S1). To our knowledge, Fig. 4d represents the longest demonstration of continuous thermogalvanic output under load yet presented in the literature, and the first to reach >1 week timescales. We note that in the absence of [TBA][PF<sub>6</sub>], the cell exhibits comparatively poor stability, steadily declining from ~0.2 V to ~0.060 V after eight days, with the current dropping from ~0.5 mA to ~0.1 mA (Fig. S14). This comparison highlights the critical role of PF<sub>6</sub><sup>-</sup> in regulating the solvation environment. By stabilizing Ni(III), disrupting rigid coordination shells, enabling greater entropy change during redox cycling, and accelerating [Ni(bpy)<sub>3</sub>]<sup>2+/3+</sup> kinetics, it maintains efficient long-term thermogalvanic charge transfer.

Finally, in Fig. 5 we summarize the transport properties and efficiency metrics of the RS-TGC. The combination of the EC solvent and the added [TBA][PF<sub>6</sub>] result favorably in both low thermal conductivity (~0.23 W m<sup>-1</sup> K<sup>-1</sup> at Δ*T* = 75 K) and high electrical conductivity (~13.2 S m<sup>-1</sup> at Δ*T* = 75 K), each of which furthermore trend desirably with Δ*T* (as expected based on increasing average electrolyte temperature) across the wide window of evaluation (Fig. 5a). The low thermal conductivity is an intrinsic feature of non-aqueous carbonate solvents such as EC (Fig. S15),<sup>51–53</sup> provides a particular advantage over most water-based thermogalvanic systems, which generally suffer from high thermal conductivity (>0.5 W m<sup>-1</sup> K<sup>-1</sup>) and according parasitic heating.<sup>3,9</sup>

In Fig. 5b, we show the energy conversion efficiency and relative Carnot efficiency for the cell as a function of applied temperature gradient, which peak at ~1.5% and ~8.5%, respectively, at Δ*T* = 75 K. Both efficiency and power density are observed to increase with applied temperature gradient (Fig. 5c), with *P*<sub>max</sub> growing from ~1.5 W m<sup>-2</sup> at Δ*T* = 30 K to ~8 W m<sup>-2</sup> at Δ*T* = 75 K.

The exceptional Seebeck coefficient of the RS-TGC, coupled with its low thermal conductivity and high electrical conductivity, culminate in remarkably high thermoelectric figures of merit (*ZT*; ~0.5–0.83) across Δ*T* values, well above the typical *ZT* < 0.2 reported for aqueous TGCs. When compared against state-of-the-art systems (Fig. 5e), the RS-TGC reported herein occupies an as-yet touched performance region, combining both uniquely high *ZT* and high relative Carnot efficiency, as compared to the low-*ZT*, low-efficiency regime occupied by most conventional TGCs (Table. S1).

## Conclusion

This study employs the [Ni(bpy)<sub>3</sub>]<sup>2+</sup>/[Ni(bpy)<sub>3</sub>]<sup>3+</sup> couple to introduce the concept of a redox-split thermogalvanic cell (RS-TGC), a new paradigm for liquid-phase thermoelectric systems. Unlike conventional TGCs, which remain constrained by homogeneous distributions of redox species both under isothermal and gradient conditions, RS-TGCs exploit thermally induced partitioning in which one redox species (here [Ni(bpy)<sub>3</sub>]<sup>3+</sup>) is generated selectively at one electrode (here the hot), while the other redox species ([Ni(bpy)<sub>3</sub>]<sup>2+</sup>) dominates in bulk solution. This localized oxidation creates persistent

chemical heterogeneity, amplifying both solvation-entropy and concentration-ratio contributions to thermopower.

To further enhance these effects, we also incorporate entropy-regulating anions, which spectroscopic and electrochemical evidence demonstrate disrupt rigid solvation cages, displace strongly bound Br<sup>-</sup> ions, and promote partial desolvation, thereby stabilizing the Ni(III) state. Molecular dynamics and DFT calculations also confirm that this disruption enhances both configurational and vibrational redox entropy changes, lowers reorganization energies, and increases molecular mobility, directly linking microscopic solvation behaviors to macroscopic thermoelectric response. As a result, the system achieves a Seebeck coefficient of 6.44 mV K<sup>-1</sup>, surpassing conventional redox couples including Fe<sup>3+</sup>/Fe<sup>2+</sup>, I<sup>-</sup>/I<sub>3</sub><sup>-</sup>, and BQ/HQ. Transport measurements further show that the optimized RS-TGC configuration developed herein overcomes the traditional trade-off between electrical and thermal conductivities by use of salt-supplemented ethylene carbonate electrolytes. This optimization yields a thermoelectric figure of merit approaching 0.8 and a Carnot-relative efficiency of ~8%, positioning RS-TGCs among the highest-performing liquid thermogalvanic systems reported to date. Crucially, RS-TGCs also demonstrate exceptional durability, sustaining both voltage and power output for more than ten days under continuous operation and maintaining stable responses under repeated cycling. This combination of high thermopower and multiday operability establishes RS-TGCs as an unusually durable and efficient potential platform for low-grade heat harvesting.

Importantly, the redox-partitioning strategy demonstrated here with the [Ni(bpy)<sub>3</sub>]<sup>2+/3+</sup> pair can, in principle, be extended to other systems. The key requirement qualifying a given thermogalvanic electrolyte for potential redox splitting is that a single redox species must dominate in the bulk, while radical or reduced forms may be transiently generated. For example, one promising candidate fitting this description may be benzoquinone (BQ), which remains stable in the bulk, but may undergo transient redox conversion to semiquinone/dianion (SQ<sup>2-</sup>). Looking forward, the principles of redox partitioning and entropy regulation outlined herein provide a generalizable design strategy that can be extended to new redox couples, solvent systems, and interfacial architectures, enabling scalable advances in liquid thermoelectrics.

## Methods

### Materials

Tris(2,2'-bipyridine)nickel(II) bromide ([Ni(bpy)<sub>3</sub>]Br<sub>2</sub>, 95%), propylene carbonate (PC), *N,N*-dimethylformamide (DMF), formamide (FA), acetonitrile (MeCN), ethylene carbonate (EC), and the ionic salts [BMIM][TFSI], [EMIM][TFSI], [TBA][TFSI], [BMIM][PF<sub>6</sub>], [EMIM][PF<sub>6</sub>], and [TBA][PF<sub>6</sub>] were purchased from Ambeed and used as received. Graphite sheets (resistivity ~10 Ω m, Graphite Material Co. Ltd.), carbon cloth electrodes (Hexcel IM7, ~15 Ω m), graphite felt (Fuel Cell Store, 200 m Ω cm<sup>2</sup>), and platinum sheets (99.99% purity, StonyLab) served as electrode materials.



## Cell fabrication and assembly

Thermogalvanic cells were fabricated by 3D printing with internal liquid chambers ( $10 \times 10 \times 35$  mm) and electrode-electrolyte contact areas of  $1 \text{ cm}^2$ . Graphite sheets were used for Seebeck coefficient measurements, whereas graphite felt electrodes were employed for power output experiments. Cells were sealed with silicone adhesive. Electrode temperatures were controlled by two Peltier modules ( $4 \times 4$  cm), with thermocouples placed at each electrode. Insulating tape was applied to minimize heat loss, and electrical connections were made using copper tape and wires.

## Electrolyte preparation

For each solvent, the working concentration of  $[\text{Ni}(\text{bpy})_3]\text{Br}_2$  was set to the average solubility at which the complex dissolved uniformly and remained stable: 0.05 M in PC, 0.1 M in DMF, 0.1 M in FA, 0.05 M in MeCN, and 0.2 M in EC. These concentrations ensured  $[\text{Ni}(\text{bpy})_3]^{2+}$  remained the dominant species while allowing controlled formation of  $[\text{Ni}(\text{bpy})_3]^{3+}$  at the hot electrode (Fig. 2d and S6a). Solutions were stirred at 323 K (150 rpm) for 12 h to ensure homogeneity upon preparation.

Among the solvents, EC containing 0.2 M  $[\text{Ni}(\text{bpy})_3]\text{Br}_2$  produced the highest Seebeck coefficient (Fig. 2e and S6b). To investigate the role of entropy-regulating anions, six supporting salts were introduced into EC at 0.5 M concentration: [BMIM][TFSI], [EMIM][TFSI], [TBA][TFSI], [BMIM][PF<sub>6</sub>], [EMIM][PF<sub>6</sub>], and [TBA][PF<sub>6</sub>]. These mixtures were stirred at 50 °C for 6 h. The optimized electrolyte was identified as EC containing 0.2 M  $[\text{Ni}(\text{bpy})_3]\text{Br}_2$  and 0.5 M [TBA][PF<sub>6</sub>]. To further probe concentration effects, [TBA][PF<sub>6</sub>] was varied between 0.2 M and 1.0 M. Unless otherwise specified, all electrochemical tests employed this optimized electrolyte.

## Temperature control and thermal gradient

The maximum applied temperature difference ( $\Delta T$ ) was limited to 75 K, determined by the melting and boiling points of the solvents. For EC, the cold side was maintained at 313 K and the hot side raised to 388 K. Because EC solidifies near 311 K, only liquid-phase measurements were conducted; the addition of salts also depressed the freezing point to  $\sim 303$  K, further ensuring stability during operation. For PC, DMF, and FA, temperature ranges were set at 298 K (cold side) to 373 K (hot side). For MeCN, with its lower boiling point, the range was set between 253 K and 328 K. In all cases,  $\Delta T$  was increased in 15 K increments.

## Cell characterization

Voltage and current outputs were measured with a Keithley 2000 multimeter, with continuous data acquisition performed using MATLAB scripts. Discharge experiments were monitored through a resistance board. For cycling measurements, the cell was maintained at constant  $\Delta T$  until the open-circuit voltage stabilized, followed by either short-circuiting ( $R = 0$ ) or connection to a fixed external load to simulate operating conditions.

## Author contributions

E. H., M. Z., and M. P. P. conceived the research; E. H., M. Z., and M. P. P. designed the experiments; E. H., M. Z., M. H., and R. Z. carried out the experiments; M. Z. and A. Z. conducted the physical property characterization; E. H., M. Z., and M. H. performed the computational modeling; all authors analyzed the data; E. H., M. Z., and M. P. P. wrote the paper, and all authors approved the final version.

## Conflicts of interest

M. P. P., E. H., and M. Z. have filed a patent related to this work. The other authors declare no conflicts of interest.

## Data availability

The data that support the findings of this study are available from the corresponding author upon reasonable request. All relevant experimental and computational data generated and analyzed during this study are included in the manuscript and its supplementary information file. Additional datasets related to this article will be made available upon request for academic research purposes.

Supplementary information (SI) is available. See DOI: <https://doi.org/10.1039/d5ta09239f>.

## Acknowledgements

This work and all authors were funded through the start-up funds of M. J. P.-P. in the J. Mike Walker '66 Department of Mechanical Engineering at Texas A&M University.

## References

- 1 T. Quickenden and Y. Mua, A review of power generation in aqueous thermogalvanic cells, *J. Electrochem. Soc.*, 1995, **142**(11), 3985.
- 2 X. He, *et al.*, Redox-induced thermocells for low-grade heat harvesting: mechanism, progress, and their applications, *J. Mater. Chem. A*, 2022, **10**(39), 20730–20755.
- 3 Y. Liu, *et al.*, Thermo-electrochemical cells for heat to electricity conversion: from mechanisms, materials, strategies to applications, *Energy Environ. Sci.*, 2022, **15**(9), 3670–3687.
- 4 Y. Wang, *et al.*, In situ photocatalytically enhanced thermogalvanic cells for electricity and hydrogen production, *Science*, 2023, **381**(6655), 291–296.
- 5 S. Sun, *et al.*, Advances in ionic thermoelectrics: from materials to devices, *Adv. Energy Mater.*, 2023, **13**(9), 2203692.
- 6 J. Duan, *et al.*, Aqueous thermogalvanic cells with a high Seebeck coefficient for low-grade heat harvest, *Nat. Commun.*, 2018, **9**(1), 5146.
- 7 T. J. Abraham, D. R. MacFarlane and J. M. Pringle, High Seebeck coefficient redox ionic liquid electrolytes for thermal energy harvesting, *Energy Environ. Sci.*, 2013, **6**(9), 2639–2645.



- 8 N. Jabeen, *et al.*, Recent advances in ionic thermoelectric systems and theoretical modelling, *Chem. Sci.*, 2024, **15**(35), 14122–14153.
- 9 Y. Zeng, *et al.*, Solvation entropy engineering of thermogalvanic electrolytes for efficient electrochemical refrigeration, *Joule*, 2025, **9**(3), 101822.
- 10 X. Qian, *et al.*, Thermodynamics of ionic thermoelectrics for low-grade heat harvesting, *ACS Energy Lett.*, 2024, **9**(2), 679–706.
- 11 J. Duan, *et al.*, Liquid-state thermocells: Opportunities and challenges for low-grade heat harvesting, *Joule*, 2021, **5**(4), 768–779.
- 12 B. Yu, *et al.*, Thermosensitive crystallization–boosted liquid thermocells for low-grade heat harvesting, *Science*, 2020, **370**(6514), 342–346.
- 13 H. Zhou, T. Yamada and N. Kimizuka, Supramolecular thermo-electrochemical cells: enhanced thermoelectric performance by host–guest complexation and salt-induced crystallization, *J. Am. Chem. Soc.*, 2016, **138**(33), 10502–10507.
- 14 L. Liu, *et al.*, Strong tough thermogalvanic hydrogel thermocell with extraordinarily high thermoelectric performance, *Adv. Mater.*, 2023, **35**(32), 2300696.
- 15 C.-G. Han, *et al.*, Giant thermopower of ionic gelatin near room temperature, *Science*, 2020, **368**(6495), 1091–1098.
- 16 Y. Li, *et al.*, Realizing record-high output power in flexible gelatin/GTA-KCl-FeCN 4–/3– ionic thermoelectric cells enabled by extending the working temperature range, *Energy Environ. Sci.*, 2022, **15**(12), 5379–5390.
- 17 D. Shin, *et al.*, Boosted thermogalvanic thermopower upon solid-to-liquid phase transition, *Energy Environ. Sci.*, 2024, **17**(20), 7712–7719.
- 18 S. Wang, *et al.*, High-performance cryo-temperature ionic thermoelectric liquid cell developed through a eutectic solvent strategy, *Nat. Commun.*, 2024, **15**(1), 1172.
- 19 H. Zhou, *et al.*, Supramolecular Thermo-Electrochemical Cells: Enhanced Thermoelectric Performance by Host–Guest Complexation and Salt-Induced Crystallization, *J. Am. Chem. Soc.*, 2016, **138**(33), 10502–10507.
- 20 S. Kim, *et al.*, Realizing a high-performance n-type thermogalvanic cell by tailoring the thermodynamic equilibrium, *Energy Environ. Sci.*, 2024, **17**(21), 8102–8110.
- 21 J.-Y. Baek, H. J. Seog and S.-Y. Jang, Solid-state n-type thermodiffusion-assisted thermogalvanic cells with unprecedented thermal energy conversion, *Energy Environ. Sci.*, 2025, **18**(13), 6714–6721.
- 22 Y. Zhu, *et al.*, Ultra-high performance of ionic thermoelectric-electrochemical gel cells for harvesting low grade heat, *Energy Environ. Sci.*, 2024, **17**(12), 4104–4114.
- 23 H. Y. Samayoa-Oviedo, *et al.*, Spontaneous ligand loss by soft landed [Ni (bpy) 3] 2+ ions on perfluorinated self-assembled monolayer surfaces, *Chem. Sci.*, 2024, **15**(28), 10770–10783.
- 24 J. B. Chlistunoff and A. J. Bard, Electrochemistry in liquid sulfur dioxide. 11. Oxidation of tris (2, 2'-bipyridine) nickel (2+) and spectroscopy and isolation of products, *Inorg. Chem.*, 1992, **31**(22), 4582–4587.
- 25 E. Hosseini, *et al.*, On a Continuous Aqueous Thermogalvanic Redox Agent with Anomalous Thermopower, *Nano Lett.*, 2025, **25**(31), 11986–11992.
- 26 K. Barman, *et al.*, Electrochemical Reduction of [Ni (Mebpy) 3] 2+: Elucidation of the redox mechanism by cyclic voltammetry and steady-state voltammetry in low ionic strength solutions, *Chemelectrochem*, 2020, **7**(6), 1473–1479.
- 27 O. Buriez, L. M. Moretto and P. Ugo, Ion-exchange voltammetry of tris (2, 2'-bipyridine) nickel (II), cobalt (II), and Co (salen) at polyestersulfonated ionomer coated electrodes in acetonitrile: Reactivity of the electrogenerated low-valent complexes, *Electrochim. Acta*, 2006, **52**(3), 958–964.
- 28 S. Derien, E. Dunach and J. Perichon, From stoichiometry to catalysis: electroreductive coupling of alkynes and carbon dioxide with nickel-bipyridine complexes. Magnesium ions as the key for catalysis, *J. Am. Chem. Soc.*, 1991, **113**(22), 8447–8454.
- 29 Z. Mtshali and J. Conradie, Tris (polypyridine) nickel (II) complexes: Synthesis, DFT and electrochemistry, *Inorg. Chim. Acta*, 2023, **549**, 121422.
- 30 R. R. Nazmutdinov, *et al.*, Ligand and solvent effects on the kinetics of the electrochemical reduction of Ni (II) complexes: Experiment and quantum chemical modeling, *Electrochim. Acta*, 2021, **395**, 139138.
- 31 N. Mateyise, M. Conradie and J. Conradie, Electrochemical and theoretical study of nickel (II) containing different 2, 2': 6', 2''-terpyridines, *Polyhedron*, 2024, **259**, 117075.
- 32 S. H. Strauss, The search for larger and more weakly coordinating anions, *Chem. Rev.*, 1993, **93**(3), 927–942.
- 33 M. Watanabe, *et al.*, Application of ionic liquids to energy storage and conversion materials and devices, *Chem. Rev.*, 2017, **117**(10), 7190–7239.
- 34 Y. Katayama, Y. Toshimitsu and T. Miura, Electrode kinetics of the redox reaction of tris (2, 2'-bipyridine) nickel complexes in an ionic liquid, *Electrochim. Acta*, 2014, **131**, 36–41.
- 35 Y. Katayama, Y. Toshimitsu and T. Miura, Electrode kinetics of tris (2, 2'-bipyridine) ruthenium complexes in 1-ethyl-3-methylimidazolium tetrafluoroborate ionic liquid, *J. Electrochem. Soc.*, 2013, **160**(4), H224.
- 36 B. J. Henne and D. E. Bartak, Metal-vapor synthesis and electrochemistry of bis (bipyridyl) nickel (0), *Inorg. Chem.*, 1984, **23**(3), 369–373.
- 37 Q. Huang, *et al.*, Simultaneously Modulating Solvation and Water Structure for High-Performance Antifreezing n-Type Liquid Thermocells, *ACS Mater. Lett.*, 2025, **7**(4), 1219–1227.
- 38 S. M. Jung, *et al.*, Fe–N–C Electrocatalyst for Enhancing Fe (II)/Fe (III) Redox Kinetics in Thermo-Electrochemical Cells (Adv. Funct. Mater. 45/2023), *Adv. Funct. Mater.*, 2023, **33**(45), 2370268.
- 39 J. Wang, *et al.*, Ultrastrong, flexible thermogalvanic armor with a Carnot-relative efficiency over 8%, *Nat. Commun.*, 2024, **15**(1), 6704.
- 40 P. F. Salazar, *et al.*, Enhanced thermo-electrochemical power using carbon nanotube additives in ionic liquid redox electrolytes, *J. Mater. Chem. A*, 2014, **2**(48), 20676–20682.



- 41 A. Taheri, *et al.*, Flexible and non-volatile redox active quasi-solid state ionic liquid based electrolytes for thermal energy harvesting, *Sustain. Energy Fuels*, 2018, 2, 1806–1812.
- 42 A. Taheri, *et al.*, Quasi-solid-state electrolytes for low-grade thermal energy harvesting using a cobalt redox couple, *ChemSusChem*, 2018, 11(16), 2788–2796.
- 43 B. Yu, *et al.*, Cost-effective n-type thermocells enabled by thermosensitive crystallizations and 3D multi-structured electrodes, *Nano Energy*, 2022, 93, 106795.
- 44 Y. Liang, *et al.*, High positive seebeck coefficient of aqueous I<sup>-</sup>/I<sub>3</sub><sup>-</sup> thermocells based on host-guest interactions and LCST behavior of PEGylated  $\alpha$ -cyclodextrin, *ACS Appl. Energy Mater.*, 2021, 4(5), 5326–5331.
- 45 J. Duan, *et al.*, PN conversion in thermogalvanic cells induced by thermo-sensitive nanogels for body heat harvesting, *Nano Energy*, 2019, 57, 473–479.
- 46 K. Kim and H. Lee, Thermoelectrochemical cells based on Li<sup>+</sup>/Li redox couples in LiFSI glyme electrolytes, *Phys. Chem. Chem. Phys.*, 2018, 20(36), 23433–23440.
- 47 D. J. Szalda, *et al.*, Electron-transfer barriers and metal-ligand bonding as a function of metal oxidation state. 2. Crystal and molecular structures of tris (2, 2'-bipyridine) cobalt (II) dichloride-2-water-ethanol and tris (2, 2'-bipyridine) cobalt (I) chloride-water, *Inorg. Chem.*, 1983, 22(17), 2372–2379.
- 48 J. Li, *et al.*, Confined phase transition triggering a high-performance energy storage thermo-battery, *Energy Environ. Sci.*, 2024, 17(18), 6606–6615.
- 49 J. Hu, *et al.*, Double selective ionic gel with excellent thermopower and ultra-high energy density for low-quality thermal energy harvesting, *Energy Environ. Sci.*, 2024, 17(5), 1664–1676.
- 50 K. Laws, *et al.*, High Seebeck coefficient thermogalvanic cells via the solvent-sensitive charge additivity of cobalt 1, 8-diaminosarcophagine, *Chem. Commun.*, 2023, 59(16), 2323–2326.
- 51 M. Atilhan and S. Aparicio, A review on the thermal conductivity of deep eutectic solvents, *J. Therm. Anal. Calorim.*, 2023, 148(17), 8765–8776.
- 52 Z. Cheng, *et al.*, Ionic Peltier effect in Li-ion electrolytes, *Phys. Chem. Chem. Phys.*, 2024, 26(8), 6708–6716.
- 53 C. L. Yaws, *Handbook of Thermal Conductivity: Organic Compounds C1 to C4*, Gulf Professional Publishing, Vol. 1. 1995.
- 54 D. Zhang, *et al.*, Stretchable thermogalvanic hydrogel thermocell with record-high specific output power density enabled by ion-induced crystallization, *Energy Environ. Sci.*, 2022, 15(7), 2974–2982.
- 55 G. Li, *et al.*, High-efficiency cryo-thermocells assembled with anisotropic holey graphene aerogel electrodes and a eutectic redox electrolyte, *Adv. Mater.*, 2019, 31(25), 1901403.
- 56 T. Kim, *et al.*, High thermopower of ferri/ferrocyanide redox couple in organic-water solutions, *Nano Energy*, 2017, 31, 160–167.
- 57 T. J. Kang, *et al.*, Electrical power from nanotube and graphene electrochemical thermal energy harvesters, *Adv. Funct. Mater.*, 2012, 22(3), 477–489.
- 58 Z. Lei, W. Gao and P. Wu, Double-network thermocells with extraordinary toughness and boosted power density for continuous heat harvesting, *Joule*, 2021, 5(8), 2211–2222.
- 59 L. Zhang, *et al.*, High Power Density Electrochemical Thermocells for Inexpensively Harvesting Low-Grade Thermal Energy, *Adv. Mater.*, 2017, 29(12), 1605652.

